Received: 13 October 2022 | Revised: 13 March 2023 | Accepted: 22 April 2023

DOI: 10.1002/cnm.3718

APPLIED RESEARCH

WILEY

The effect of thoracic dimensions on compression depth during cardiopulmonary resuscitation

Jafar Moradicheghamahi[1] | **Gerard Fortuny**[1] | **Josep M. López**[1] | **Dolors Puigjaner**[1] | **Joan Herrero**[2] | **Youcef Azeli**[3,4,5]

[1]Departament d'Enginyeria Informàtica i Matemàtiques, Universitat Rovira i Virgili, Tarragona, Catalunya, Spain

[2]Departament d'Enginyeria Química, Universitat Rovira i Virgili, Tarragona, Catalunya, Spain

[3]Sistema d'Emergències Mèdiques de Catalunya, L'Hospitalet de Llobregat, Barcelona, Spain

[4]Emergency Department, Hospital Universitari Sant Joan de Reus, Reus, Tarragona, Spain

[5]Institut d' Investigació Sanitària Pere i Virgili (IISPV), Tarragona, Spain

Correspondence
Gerard Fortuny, Departament d'Enginyeria Informàtica i Matemàtiques, Universitat Rovira i Virgili, Tarragona, Catalunya, Spain.
Email: gerard.fortuny@urv.cat

Funding information
Universitat Rovira i Virgili, Grant/Award Number: 2018PFR-URV-B2-29

Abstract

The effect of the dimensions of the thoracic cage on the resuscitation outcome of cardiopulmonary resuscitation (CPR) maneuvers has long been debated. In this study, the effect of changes in the rib cage dimensions on the achieved compression depth was investigated using finite element simulations. A total of 216 different rib cage geometry models were considered and, in each case, the result of applying different levels of compression force up to 600 N were simulated. The Haller Index of the rib cage is defined as the ratio of the transverse diameter and the antero-posterior diameter. Our results suggest that, with a fixed level of compression force, performing CPR on rib cages having a low Haller Index and/or a larger height leads to compression depths below the average. Alternatively, if a target compression depth is set for CPR, in general a lower compression force would be required for individuals with higher Haller Index and/or lower chest height. In addition, present results indicate that wider chested individuals will experience lower stress levels on their ribs to achieve the required CPR target depth. Moreover, in the present study we propose predictive models, based on anthropometric parameters, for compression depth and rib stress during chest compressions. In particular, the model suggests that in future correlations of empirical CPR data the patients' Haller index and vertical (sagittal) cross-area are the best parameters to be used as independent variables in a fit.

KEYWORDS

cardiac arrest, cardiopulmonary resuscitation (CPR), finite element method, Haller index

1 | INTRODUCTION

Survival of cardiac arrest hardly exceeds 10% despite the research efforts made over the last two decades.[1] Compressions are the most important maneuver performed during cardiopulmonary resuscitation (CPR). The technique of chest compressions was first described in 1960 and it has remained practically unchanged hitherto.[2] In 2010, resuscitation guidelines recommended increasing the compression depth from 4 to 5 cm.[3] Later, higher survival rates were reported for compression depths between 4.03 and 5.53 cm in a large series of out-of-hospital cardiac arrests (OHCA), generating

controversy in the scientific community.[4,5] Increasing compression depth can increase cardiac output but, on the other hand, can increase the incidence of injury and worsen hemodynamics during CPR.[6,7] Thoracic CPR-related injuries have been associated with loss of thoracic elasticity and poorer survival outcomes[8] and they have recently been described as an independent factor associated with poor prognosis.[9] Recent studies based on large samples of patients concluded that the highest survival rates were associated with smaller compression depths of 4.56[4] or 4.7 cm.[10] Moreover, the notion that the dimensions of each individual patient ought to be taken into account when establishing a target compression depth for CPR is strongly supported by recent literature on the subject.[11–14]

The chance of success of the CPR maneuvers will depend, for each individual patient, on both the ratio of heart compression achieved, which will most probably increase with increasing compression depth (ΔY), and the rate of development of injuries as a result of the compressions.[7] In view that a patient-specific optimization of the target compression depth was out of question, the choice of a population-wide target depth for CPR was based on a global balance between efficiency (maximizing heart compression) and safety (minimizing injuries). Assessing the risk of fracture based on the dimensions of the patient may be helpful in personalizing compression depths. Some patients may benefit from greater compression depths, however in other cases compression depths should be limited.

Numerical simulations are no doubt a valuable complement to experimental studies on CPR, which are quite often performed on human corpses. Finite element (FE) simulations provide, at a relatively low cost, the ability to simulate different conditions and to predict the effect of changes in the model parameters. Recently, Suazo et al.[15] used a FE approach to simulate the effect of changes in the CPR compression location on the response experienced by an adult rib cage. The aim of the present study is to perform FE simulations of rib cage compression on a set of differently sized adult models and, on the basis of the numerical results obtained, to develop predictive models for the achieved compression depth and rib stress during CPR maneuvers.

2 | MODELS AND METHODS

The present study is based on the model and methods previously implemented in Reference [15], which will be summarized in what follows for the sake of completeness. The geometry model, sketched in Figure 1A,B, comprises the breastbone, the costal cartilages, the osseous ribs and the intercostal muscles. The vertebral column, also shown in Figure 1A, is part of the geometry model but it plays no role in the FE simulations as fixed boundary conditions are prescribed in the locations where the costo-vertebral joints meet the column. The geometry model was generated as a refinement of a previous raw model available in the BodyParts3D database for anatomy, which was in turn obtained by segmentation of CT images of an adult man.[16] The computational mesh resulting from the discretization of the refined geometry model consisted of 1,006,571 nodes and 5,624,647 linear elements (1,235,972 triangles and 4,388,675 tetrahedrals). The

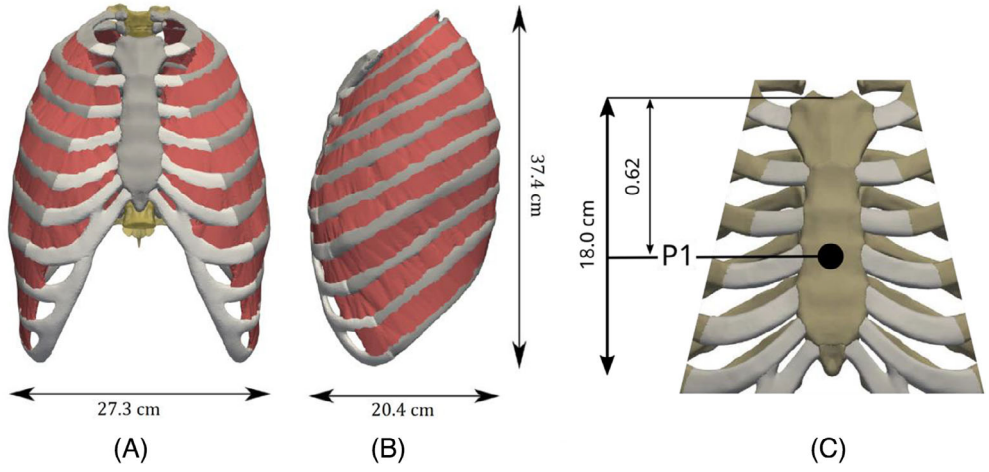

FIGURE 1 Sketch of the geometry model used in the present study. (A) Frontal view of the rib cage, showing the breastbone, costal cartilages, osseous ribs, and the nine pairs of intercostal muscle sections. The vertebral column is also shown even though this element plays no role in the simulations because of the fixed boundary condition assumed. (B) Sagittal view. (C) Magnification of the region around the breast+bone in (A). Intercostal muscles are colored in red, breastbone and osseous ribs in dark gray and cartilages are denoted with a lighter gray. The location of the center of the compression area (P1), expressed as a ratio of the breastbone length, is also shown in (C).

compression force is applied into a small patch (some 10 cm^2 in area) on the outer surface of the breastbone (the region referred to as P1 in.[15]; see Figure 1C). Simulations were performed using the Code Aster open source software.[17]

2.1 | Constitutive material models

The different tissues are modeled as homogeneous materials, and in most cases linearly elastic (see Table 1). A linear isotropic elastic behavior is set for the costal cartilages. It is well established that the Young modulus of the cartilage (E_c) strongly depends on its degree of calcification,[18,19] which usually increases with age.[20,21] Forman[18] proposed a mathematical relation between E_c and McCormick's calcification score (CS).[20] In the present study, we assume a CS value of 1.5 for the costal cartilages, which leads to $E_c = 27$ MPa according to Forman's formula. Suazo et al.[15] showed that using this E_c value, together with a Poisson ratio of $\eta_c = 0.45$ for the cartilage, the linear elastic model reproduced fairly well the experimental test results of Forman and Kent.[22]

It is important to note that the mechanical properties of osseous tissues are known to be anisotropic. Some recent works[23–25] show how to systematically evaluate a map of the bone anisotropic directions from micro-CT scans, provided a high enough image resolution (a few tens of a μm). However, because of the high-radiation levels involved, micro-CT scans of an adult ribcage can only be obtained postmortem.[26] Thus, in the absence of a mapping of the osseous tissue organization, we opted for a simplified homogeneous model, which can nonetheless characterize reasonably well the mean mechanical response of the ribs and breastbone. In the present study, the bone tissue (breastbone, ribs) is assumed to follow a von Mises elastoplastic behavior with linear isotropic hardening.[27] One may say that elastoplasticity is an intermediate between two extreme behaviors, the purely elastic (spring-like) and the purely plastic (fluid-like) models.[28] The elastic-like deformation of the bone tissue occurs whenever the stress is within the tensile yield strength limit (σ_Y), while the elastoplastic deformation emerges whenever the stress reaches the yield limit. At the initiation of plastic deformation of the bone tissue, there will be a sharp reduction in the stiffness modulus (E_T), as compared to the prior elastic modulus (E_b). Note that in a process of elastoplastic deformation only part of the total stress work will be recoverable as elastic-like energy stored in the body, while the rest will be irrecoverable. Therefore, with removal of the loading only partial recovery of the shape change of the material body will be expected, and a permanent shape change will be generated.[28] In the present study, the parameters used in the elastoplastic model for the bone tissue are $E_b = 7$ GPa, $\eta_b = 0.45$, $\sigma_Y = 30$ MPa and $E_T = 2$ GPa. Suazo et al.[15] showed that these parameter values produced good simulations of the rib bending experiments previously reported by Kindig et al.[29]

Following Suazo et al.,[15] in the present study the costo-vertebral joints are modeled as capsule-like volumes of a softer material appended to the rear tip of the ribs. The capsule material was assumed to behave as an elastic solid, with a Young modulus of $E_j = 1$ MPa and a Poisson ratio of $\eta_j = 0.45$. The intercostal muscles tissue is characterizeed as a linear isotropic elastic solid with a Young modulus of $E_m = 2$ MPa and a Poisson ratio of $\eta_m = 0.49$.

As discussed by Suazo et al., the present E_m value is set to higher than the one prescribed by Kindig et al.[30] ($E_m = 1.03$ MPa) in order to incorporate the additional stiffness that would be provided by internal tissues and viscera, which are not included in the present geometry model.

2.2 | Geometry models

Table 2 summarizes the main features of the geometry model[15] that was used as the base model for the present study. The values of other geometrical quantities that are commonly used in the literature on the subject[31,32] are also included

TABLE 1 Parameters of the linear elastic models for the different tissues considered in the present study.

Tissue	Young modulus (MPa)	Poisson ratio
Costal cartilages	27	0.45
Breastbone, osseous ribs (elastic component)	7000	0.45
Costo-vertebral joints (capsule)	1	0.45
Intercostal muscles	2	0.49

Note: There are two additional parameters in the elastoplastic model for the osseous tissue, namely the tensile yield strength ($\sigma_Y = 30$ MPa) and the tangent modulus ($E_T = 2000$ MPa).

TABLE 2 Dimensions of the base geometry model and range of each of the geometrical parameters investigated in the simulations.

Parameter	Value	Range investigated
Rib cage width, W_R (cm)	27.3	22.9–28.4
Rib cage depth, L_R (cm)	20.4	15.5–21.4
Rib cage height, H_R (cm)	37.4	31.4–38.9
Transverse diameter, D_T (cm)	25.0	21.0–26.0
Antero-posterior diameter, D_{AP} (cm)	11.7	8.9–12.3
Haller index, HI (Figure 2A)	2.13	1.70–2.91
Rib angle, θ (degree)	50.9	56.9–41.9
Rib cage volume, V (dm^3) $= W_R \times L_R \times H_R$	20.8	11.1–23.7
Horizontal (axial) cross-section area A_{XY} (cm^2) $= W_R \times L_R$	556.9	355.5–608.1
Frontal (X-Z) cross-section area A_{XZ} (cm^2) $= W_R \times H_R$	1021.0	720.4–1104.3
Sagittal (Y-Z) cross-section area A_{YZ} (cm^2) $= D_{AP} \times H_R$	763.0	487.1–833.2

Note: The ranges for rib cage width, depth and height were chosen in agreement with experimental data available in the literature.[33,34]

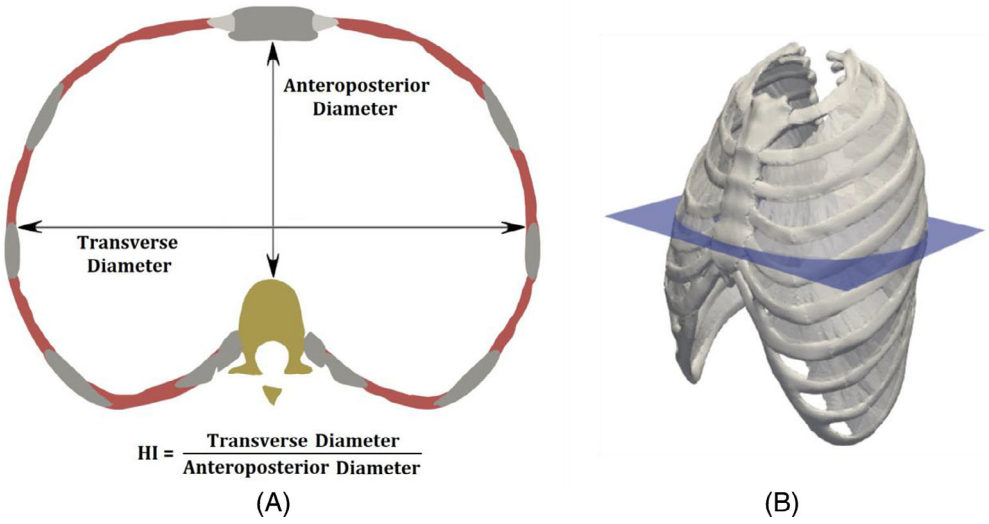

FIGURE 2 Sketch illustrating the definition of the antero-posterior (D_{AP}) and transverse (D_T) diameters used in the calculation of the Haller Index.[31,32] The height of the horizontal slice was chosen at an axial location whereby the fifth rib joints the breastbone, as shown in (B).

in Table 2. The values of the antero-posterior diameter (D_{AP}), the transverse diameter (D_T) and the Haller Index (HI) have been determined as sketched in Figure 2. The rib angle with respect to the vertical axis (θ), was measured at the height of the ninth rib.

Up to a total of 216 different geometry models were considered in the present study. The 215 new models were generated by independently stretching or compressing the base model along one of the spatial axes (X, Y, Z), as specified in Table 3.

3 | RESULTS

On each of the 216 geometry models, simulations were performed for 12 different values of the compression force, from $F = 50$ to 600 N, with an incremental step of 50 N. The simulation results are analyzed in what follows with a first

TABLE 3 Ratios of stretching/shortening applied along the X (δX), Y (δY), and Z (δZ) directions.

δX	%	Rib cage width (cm)	δY	%	Rib cage depth (cm)	δZ	%	Rib cage height (cm)
0.84	84	22.9	0.76	76	15.5	0.84	84	31.4
0.88	88	24.0	0.82	82	16.7	0.88	88	32.9
0.92	92	25.1	0.88	88	18.8	0.92	92	34.4
0.96	96	26.2	0.94	94	19.6	0.96	96	35.9
1	100	27.3	1	100	20.4	1	100	37.4
1.04	104	28.4	1.05	105	21.2	1.04	104	38.9

Note: A total of $6 \times 6 \times 6 = 216$ geometries were considered. The resulting values of the rib cage width (W_R), rib cage depth (L_R) and rib cage height (H_R) are included in the table for the sake of clarity. The proportions of the median individual would be $\delta X = 0.94$ (94%), $\delta Y = 0.905$ (90.5%), and $\delta Z = 0.94$ (94%).

subsection focused in the achieved compression depth and a second subsection dealing with the stress levels experienced by the ribs as a result of the compression.

3.1 | Compression depth as a function of the problem parameters

Figure 3 shows the effect of rib cage dimensions on the compression depth achieved on the location P1, ΔY_{P1}, when a force of $F = 600$ N is applied. We can see in this figure that increasing either the rib cage depth or its height has a negative influence on the achieved compression depth (ΔY) whereas increasing the rib cage width leads to an increase in ΔY. The dependence of the compression depth on the rib cage dimensions and the compression force applied (F) was quantified using a least squares fit in the form $\Delta Y = \Delta Y$ (F, δX, δY, and δZ). In particular, the classical functionality of products of powers was found to produce good fits for compression forces in the 450 N $\leq F \leq$ 600 N range,

$$\Delta Y = C F^{\alpha} \delta X^{\beta} \delta Y^{\gamma} \delta Z^{\epsilon}, \tag{1}$$

where the C, α, β, γ, and ε constants of the fit were determined in each case using the FE simulations for all of the 216 geometry models. Note that values of the compression force in the 450 N $\leq F \leq$ 600 N range are commonly applied in real CPR procedures.[8] The fit obtained for the predicted maximum compression depth at the P1 compression location (ΔY_{P1}) is:

$$\Delta Y_{P1}(\text{cm}) = 0.0398 F^{0.757} \delta X^{0.552} \delta Y^{-0.763} \delta Z^{-0.306} \pm 0.0370 \text{ cm}, 450 \text{ N} \leq F \leq 600 \text{ N}. \tag{2}$$

The fit in Equation (2) confirms the qualitative behavior observed in Figure 3. Note that the stronger dependence of ΔY_{P1} on the geometry parameters, with a negative exponent of −0.763, is on rib cage depth, followed by rib cage width (a positive exponent of 0.552) and rib cage height (an exponent of −0.286). Note also that the absolute sum of the negative exponents on δY and δZ is almost twice as large as the value of the δX exponent. This means that for a hypothetical change in rib cage volume in which the X-, Y- and Z- relative proportions were kept fixed, the smaller the volume of the rib cage is the larger the compression depth achieved would be.

The corresponding fit obtained for the maximum compression depth predicted at the location P2, placed roughly midway between P1 and the xiphoid process,[15] is given by:-

$$\Delta Y_{P2}(\text{cm}) = 0.0538 F^{0.729} \delta X^{0.552} \delta Y^{-0.724} \delta Z^{-0.286} \pm 0.0471 \text{ cm}, \ 450 \text{ N} \leq F \leq 600 \text{ N}. \tag{3}$$

Note that the fit of Equation (3) is qualitatively equivalent, in regard of the signs and proportions of the powers, to that of Equation (2) for the P1 compression location.

The good quality of the fits in Equations (2) and (3), characterized by a low value of the rms error (0.0370 and 0.0471 cm, respectively), is visually depicted in Figure 4. In these graphics, the result of the fit is plotted against the value predicted by the FE simulation for each of the 216 geometry models, with the four F levels considered in the fit for each model. Figure 4 also shows that for a given geometry and F level the compression depth achieved in the

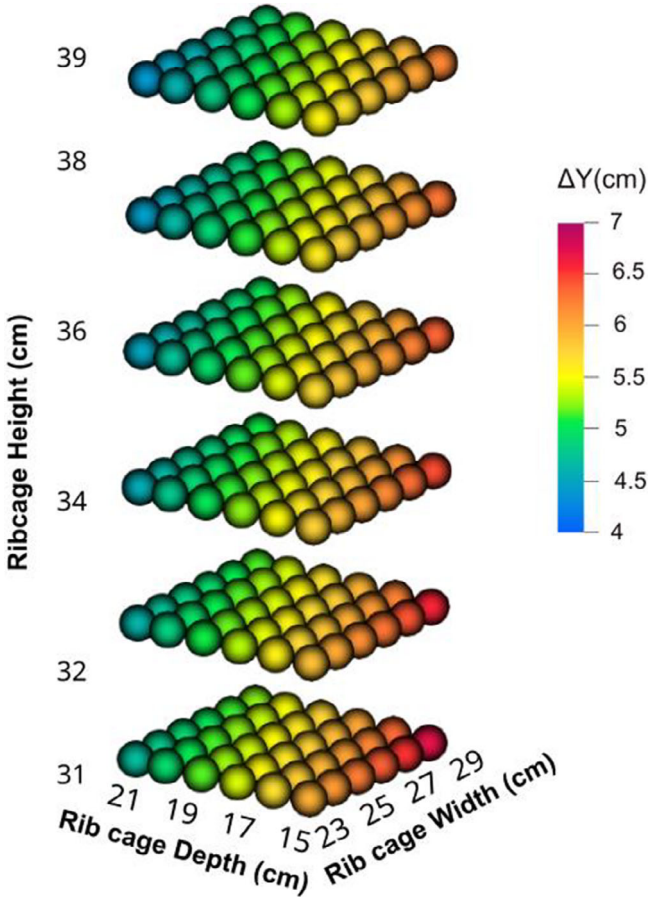

FIGURE 3 Three-dimensional scatter graph of calculated compression depth on the P1 area for all the geometry models when the compression force was $F = 600$ N. In this three-dimensional scatter diagram, each sphere represents one geometry model, and each axis represents a dimension of the rib cage. The color of each sphere indicates the compression depth achieved in that particular model, with ΔY_{P1} levels as shown in the accompanying color box.

P2 location is slightly higher (about 0.5 cm, on the average) than in P1. This result is a consequence of the so-called hinge mechanism,[15,35] which relies on the notion that during the CPR maneuver the breastbone is, basically, superiorly fixed.

3.2 | Maximum stress levels in ribs as a function of the problem parameters

In addition to the displacements as a result of the compression, the present FE simulations also yield a prediction of the stress distribution along the tissues. The von Mises stress criterion, although not very realistic, may be the most accurate for predicting fracture location when isotropic material properties are used.[36] Suazo et al.[15] showed that the calculated von Mises stress, σ_v, was especially high in the 3rd–6th osseous ribs. As an example, Figure 5 shows the predicted distributions of σ_v, on the surface of the 3rd to 6th left ribs for three different geometry models and a compression force of $F = 600$ N.

Figure 5 illustrates the fact that as the rib cage depth is increased the maximum stress levels on the ribs decrease. We assessed the effect of geometry changes on the resulting stress levels by means of a fit using the FE results from the 216 geometry models. We assumed, for each particular rib, a fit in the form of products of powers,

$$\sigma_v(\text{MPa}) = AF(\text{N})^b \delta X^c \delta Y^d \delta Z^e(\text{MPa}), 450\ \text{N} \le F \le 600\ \text{N}. \quad (4)$$

Table 4 shows the values obtained for the A, b, c, d, and e parameters in the fits of Equation 4 for the 3rd to 6th left ribs.

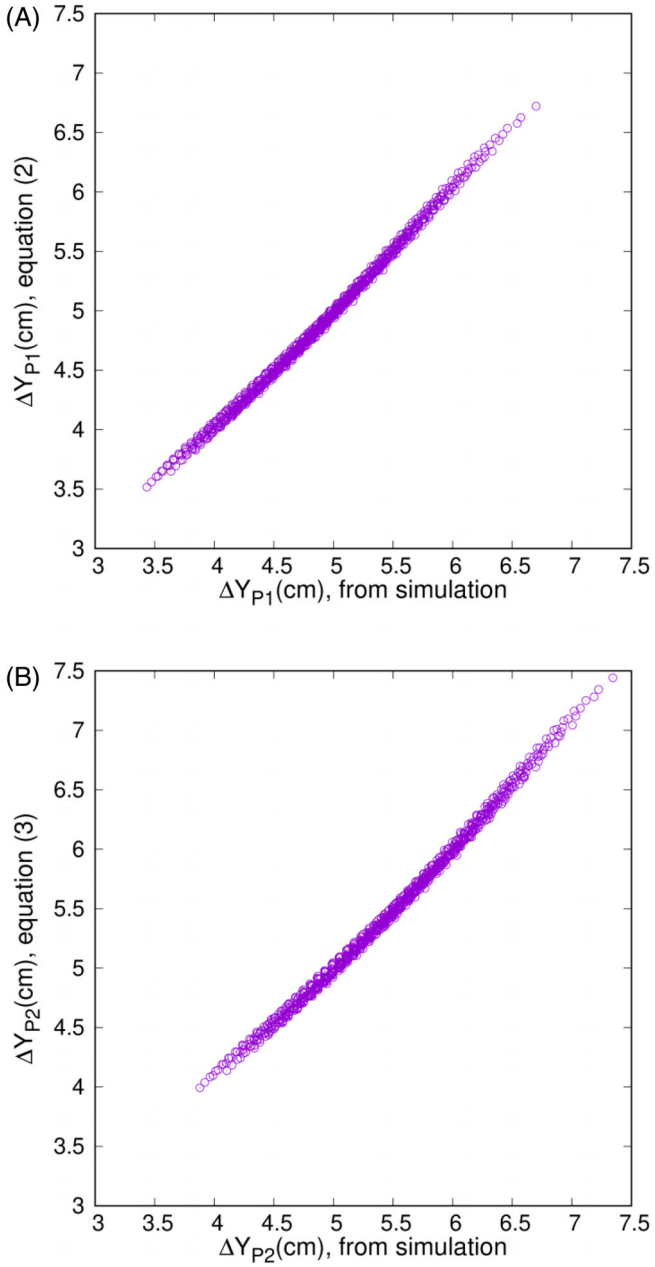

FIGURE 4 Accuracy of the fits for the predicted compression depth (ΔY) measured at (A) the compression area (P1, Figure 1) and (B) the alternative area P2 (midway between P1 and the xiphoid process).[15]

4 | DISCUSSION

The generic form of the fit given in Equation (1) is especially relevant as it provides a guide on how to proceed in future statistical analyses of empirical data on CPR. That is, we can assess which of the physical quantities describing the geometry of the patient rib cage (see Table 2) ought to be chosen to characterize the dependence of the measured compression depth (ΔY) on the rib cage dimensions. The rib cage volume, $V = W_R \times L_R \times H_R$, would not be a good candidate because of the sign variation in the exponents of δX, δY, and δZ in the fit of Equation (2). That is, given a certain variation of rib cage volume, the result of Equation (2), measured in terms of an increase or decrease on the compression depth, would depend on the way V is changed. For example, if V was increased by just increasing the rib cage width by 10% then, according to Equation (2), ΔY would increase by 5.4% ($1.1^{0.552} = 1.054$). But if the 10% increase in V was produced instead by just increasing the rib cage depth, then ΔY would not increase at all but rather decrease by 7% (as $1.1^{-0.753} = 0.930$). Using the same line of reasoning, it is easy to see that Equation (2) suggests that neither the

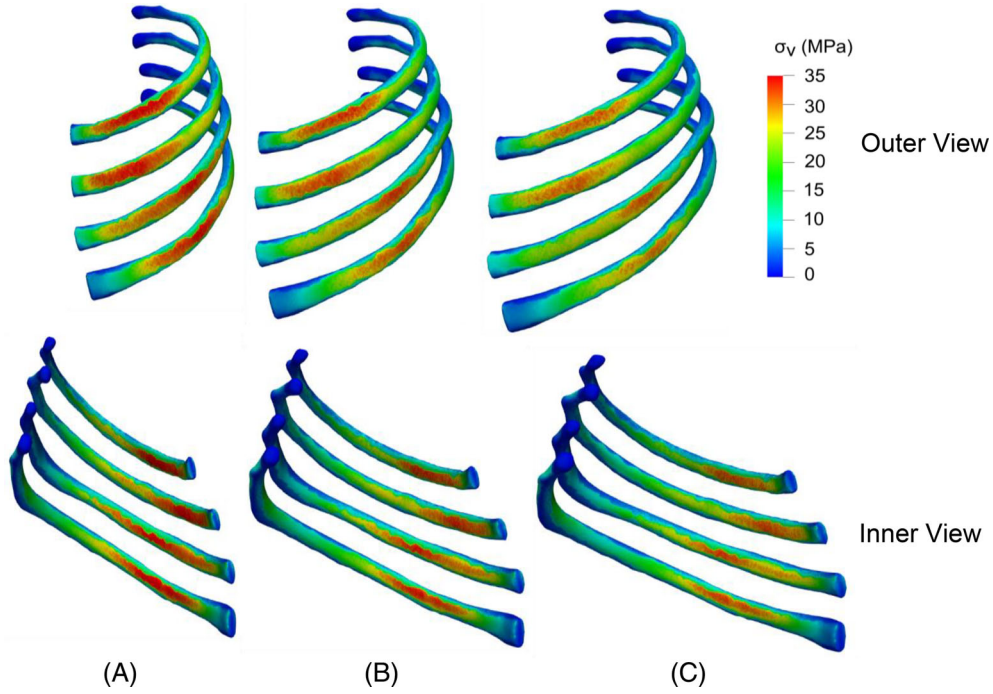

FIGURE 5 Distribution of von Mises stress (σ_v) on the surface of the 3rd, 4th, 5th, and 6th left ribs for the geometry models with $\delta X \times \delta Y \times \delta Z = 1 \times 0.76 \times 1$ (A), $1 \times 0.94 \times 1$ (B) and $1 \times 1.05 \times 1$ (C) when the compression force is $F = 600$ N. The outer and inner views of the ribs are respectively shown in the top and bottom rows of the figure.

TABLE 4 Values of the parameters in Equation (4) for the 3rd, 4th, 5th, and 6th left ribs.

Rib	*A*	*b*	*c*	*d*	*e*	rms (MPa)
3L	1.895	0.457	−0.113	−0.370	−0.445	0.370
4L	1.535	0.484	−0.310	−0.353	−0.331	0.368
5L	1.210	0.526	−0.348	−0.418	−0.311	0.439
6L	1.288	0.514	−0.285	−0.504	−0.267	0.338

Note: For a given value of the applied compression force, *F*, the maximum stress levels on the ribs (σ_v) always are found to decrease with increasing rib cage dimensions as the *c*, *d*, and *e* exponents always take negative values.

horizontal cross-section area ($A_{XY} = W_R \times L_R$) nor the vertical frontal cross-area ($A_{XZ} = W_R \times H_R$) ought to be used in correlating empirical data on ΔY. In addition, if the change in the rib angle (θ) can be approximated by the change in its tangent it follows that $\delta\theta \approx \delta(\tan\theta) = \delta Y/\delta Z$. Thus, as the exponents of δY and δZ in Equation (2) have the same sign it follows that the rib angle is neither a good candidate to correlate ΔY variations.

On the positive side, we can indeed consider the use of two other physical quantities listed in Table 2 that is, the Haller index and the sagittal cross-section area. Variations of the Haller index (HI, see Figure 2A) and of the sagittal cross-section area (A_{YZ}) can be respectively expressed as $\delta\text{HI} = \delta X/\delta Y$ and $\delta A_{YZ} = \delta Y \times \delta Z$. Thus, according to the signs of the exponents in Equation (2), these two derived quantities would be good candidates for use in a ΔY empirical correlation. To visualize this idea, let us recast Equation (2) in terms of HI and A_{YZ} instead of δX and δY:

$$\Delta Y_{P1}(\text{cm}) = 0.0398 F^{0.757} \delta\text{HI}^{0.552} \delta A_{YZ}^{-0.211} \delta Z^{-0.095} \pm 0.0370 \text{ cm}, 450 \text{ N} \le F \le 600 \text{ N}. \quad (5)$$

There are two indicators of the higher merit of Equation (5), from a statistical point of view, compared to the original Equation (2). First, the decrease in the sum of the absolute values of the exponents on the geometrical quantities, 1.621 in Equation (2) and just 0.858 in Equation (5), which would imply a lower propagation of random measurement error if empirical data had to be fitted. Second, the exponent in the least significant geometrical parameter in Equation (5) is near zero (−0.095 on δZ). Moreover, the plot in Figure 6 shows the additional convenience of

Equation (5) as it suggests a compact graphical representation of the numerical results obtained in all the present FE simulations (with forces in the 450 N ≤ F ≤ 600 N range).

Moreover, the low (absolute) exponent of δZ in Equation (5) suggests that a reasonably accurate correlation of empirical data might be obtained if Equation (5) were simplified to $\Delta Y = \Delta Y(F, \mathrm{HI}, A_{YZ})$ that is, if the explicit dependence of ΔY on the rib cage height was neglected. The corresponding fit when the dependence of ΔY on δZ is ignored is given by:

$$\Delta Y_{P1}(\mathrm{cm}) = 0.0397 F^{0.757} \delta \mathrm{HI}^{0.513} \delta A_{YZ}^{-0.267} \pm 0.0443\,\mathrm{cm}, 450\ \mathrm{N} \le F \le 600\ \mathrm{N}. \tag{6}$$

As expected, dropping the dependence of the achieved compression depth on δZ leads to a poorer fit of the FE simulation data, with a rms error of ±0.0443 cm in Equation (6), significantly larger than the ±0.0370 cm for the fit in Equation (5). Indeed, the three-variable model (6) can be said to be statistically meaningless compared to the original model in (5) as the Akaike information criterion (AIC) value is more than 10 units larger for the former model than it is for the latter one.[37] Nevertheless, reducing the dependence of ΔY from four to just three independent variables represents a large gain in terms of the number of data points (sample size) that would be required to obtain a fairly accurate fit.

As mentioned earlier, mechanically assisted CPR is mostly used nowadays to treat patients. In such a case, a target compression depth is fixed and the mechanical device exerts the compression force ($F_{\Delta Y}$) needed to achieve the target ΔY. Even though each of the present simulations has been set up for a fixed F level (a setup more representative of a manual CPR procedure), the fits in Equations (2), (5) and (6) can also be used to interpolate. For a target $\Delta Y = 5$ cm value, the fits for $F_{5\mathrm{cm}}$ corresponding to Equations (2), (5) and (6) respectively are:

$$F_{5\mathrm{cm}}(\mathrm{N}) = 590.3 \delta X^{-0.712} \delta Y^{0.989} \delta Z^{0.404} \pm 5.29\mathrm{N}, \tag{7a}$$

$$F_{5\mathrm{cm}}(\mathrm{N}) = 590.3 \delta \mathrm{HI}^{-0.712} \delta A_{YZ}^{0.277} \delta Z^{0.128} \pm 5.29\mathrm{N}, \tag{7b}$$

$$F_{5\mathrm{cm}}(\mathrm{N}) = 591.5 \delta \mathrm{HI}^{-0.658} \delta A_{YZ}^{0.351} \pm 6.16\mathrm{N}. \tag{7c}$$

Note that the rms error of the approximate, 2-variable interpolation for $F_{5\mathrm{cm}}$ in Equation (7c) (6.16 N) is significantly higher than is the rms error in Equation (7b) (5.29 N), but the difference between these two rms values is modest indeed (0.87 N). From a purely visual point of view, the $F_{5\mathrm{cm}}$ interpolations (7b) and (7c) are compared in Figure 7. Note that in the plots of Figure 7A,B only the results of those FE simulations yielding ΔY values close to 5 cm are represented. Even though, as none of the FE simulations yielded a compression depth exactly equal to the 5 cm target,

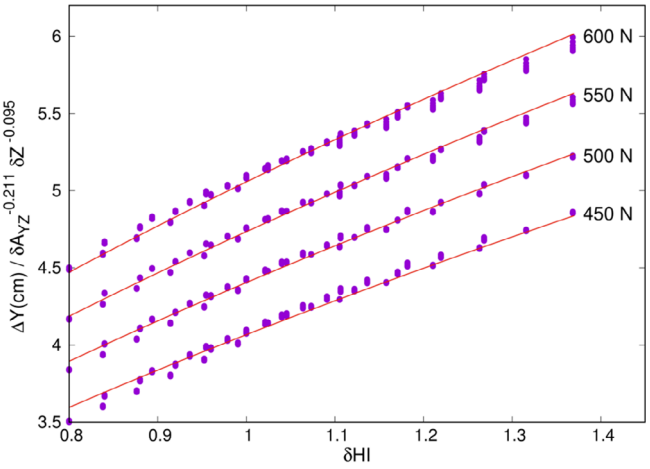

FIGURE 6 Explicit dependence of the compression height, ΔY, on the Haller Index, HI. The solid circles denote the values predicted in the simulations whereas the red lines have been plotted using the fit in Equation (5) that is, they denote the values of the function $G(F, \mathrm{HI}) = 0.0398\ F^{0.757}\ \delta \mathrm{HI}^{0.552}$.

a certain dispersion of the data points around the interpolation line, in addition to the error inherent to the fit, is unavoidable in the plots.

Comparison of the plots in Figures 7A,B qualitatively confirms the notion that little additional error is induced by obviating the explicit dependence on δZ in Equation (7b) (even though, as discussed above, the statistical value of the approximate model in (7c) is negligible, compared to the complete model in (7b), in regard of its much higher AIC value). From a practical point of view, this simplification is highly relevant considering that the antero-posterior diameter (D_{AP}) and the transverse diameter (D_T), needed to calculate the Haller index, are quite often more easily measurable than the rib cage height (H_R) is. Note that Equations (7b) and (7c) tell us that the force needed to compress the rib cage down to a target level mainly depends, with a highly negative exponent, on the Haller index. That is, patients having a rib cage with a low Haller index would require the application of a higher compression force in CPR.

The fit in Equation (4) provides a valuable insight on the dependence on the compression force and rib cage dimensions of the maximum von Mises stress levels (σ_v) supported by the ribs during CPR. Notwithstanding, from a practical point of view it is interesting to consider what is the dependence of σ_v on the rib cage geometry when a target ΔY is set for CPR. To this purpose, we can produce the interpolation fits, based on Equation (4), by replacing the F input quantity by the ΔY output quantity. For example, in the case of the 6th left rib, we obtain:

$$\sigma_v^{(6L)}(\mathrm{MPa}) = 11.28(\Delta Y(\mathrm{cm}))^{0.689}\delta X^{-0.676}\delta Y^{0.0099}\delta Z^{-0.060} \pm 0.365\,\mathrm{MPa}, \tag{8a}$$

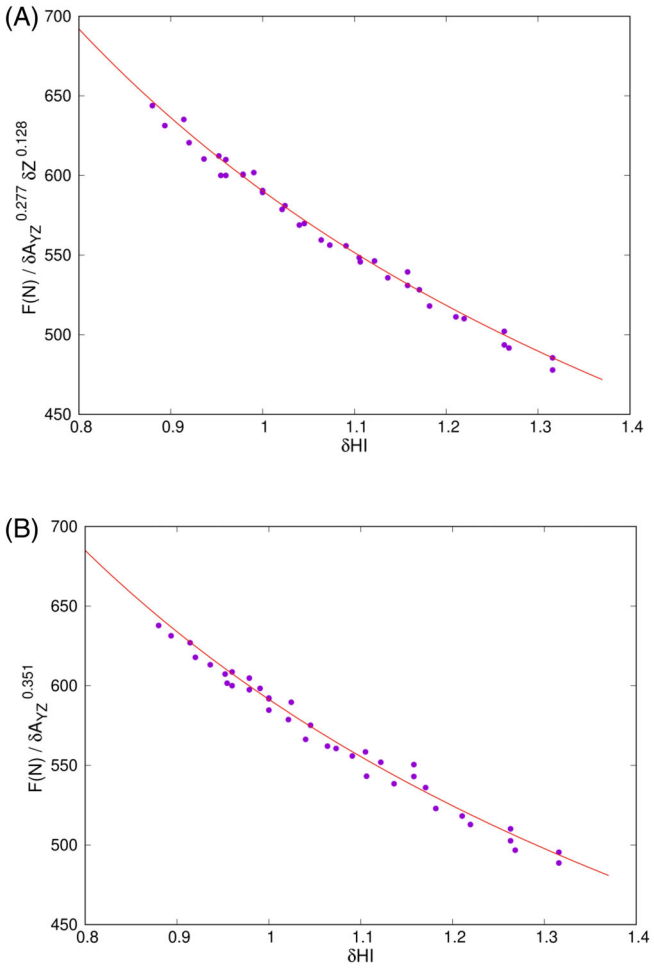

FIGURE 7 Dependence on the Haller index (HI) of the force required to achieve a target compression depth of $\Delta Y = 5$ cm at the compression area P1, F_{5cm}. Results from those simulations yielding ΔY values within 0.037 cm of the target (i.e., not further away than the rms of the fit in Equation (5)) are shown in the plots as filled circles. In (A) and (B), the solid lines respectively represent the function provided by Equations (7b) ($G(\mathrm{HI}) = 590.3\ \delta\mathrm{HI}^{-0.712}$) and (7c) ($G(\mathrm{HI}) = 591.5\ \delta\mathrm{HI}^{-0.658}$).

which for a target depth of $\Delta Y = 5$ cm yields,

$$\sigma_{v,5\mathrm{cm}}^{(6L)}(\mathrm{MPa}) = 34.22\delta X^{-0.676}\delta Y^{0.0099}\delta Z^{-0.060} \pm 0.365\,\mathrm{MPa}. \quad (8b)$$

Similar equations could be written for the rest of ribs. The exponents of such additional equations (not included here for the sake of brevity), even though different from the values in Equations (8a) and (8b), follow the same qualitative trend that is, the exponent on δX is always by far the dominant one (largest absolute value). From a purely geometrical point of view, an increase (decrease) in W_R (while keeping fixed values of L_R and H_R) means an enlargement (shortening) of the rib arc-length. Equations (8a) and (8b) are thus reflecting the fact that, in mechanical terms, an increase (decrease) of the rib arc-length induces a decrease (increase) of the resistance to bending posed by the osseous rib.

The fits in Equations (4) and (8) and, at a qualitative level, the plots in Figure 5 show that the present FE simulations do not predict a significant risk of rib fracture during CPR given that the maximum stress (σ_v) observed in the ribs is below the fracture tension limit (about $\sigma_C = 50$ MPa[15]). The empirical evidence, however, is that rib fractures do indeed occur as a consequence of CPR maneuvers[8,38,39] and some authors even suggest that chest injuries are a price worth paying to achieve optimal efficacy of chest compressions.[40] Note however that the predicted maximum σ_v values for a target CPR compression depth of 5 cm are above the $\sigma_Y = 30$ MPa yield strength limit set in the present elastoplastic model for the osseous tissue (see Equation 8b). That is, the present FE results hint at the notion that the original state of the chest would not be recovered after completing a compression cycle and that the osseous ribs tissue would slowly but inexorably deteriorate in subsequent CPR cycles.

Additionally, a more systemic interpretation of the results in Equations (4) and (8) is as follows. When a given compression force level (F) is applied during CPR two contradictory effects come into play. On one side, as F increases so does ΔY (a positive outcome) but so do as well the stress levels experienced by the ribs (negative outcome). Note that Equations (2), (3) and (5) together suggest that, as a rule, patients with a wider chest (larger W_R and larger HI) will have a higher ΔY (for a given F). In addition, Equation (4), together with the fit parameter values in Table 4, indicates that the stress levels experienced by the ribs will be indeed smaller for patients with larger chests. Equation (8) points towards the same direction for a CPR performed with a target compression depth that is, patients with a wider chest (larger W_R, and thus larger transverse diameter, D_T) will suffer smaller stress levels on their rib cage during CPR.

Azeli et al.[39] recently reported that the risk of severe chest injuries during CPR was statistically related to a larger chest circumference of the patients. The measured chest circumference is proportional to the in-plane rib arc-length, a quantity that is known to increase with the patients' age.[41] The typical changes in chest morphology with age are well established in previous studies.[41–45] Such changes basically consist in an increase of the angle of the ribs (θ), which implies an increase in the chest antero-posterior diameter (D_{AP}) together with a decrease in its transverse diameter (D_T). In other words, older patients have, on the average, their ribs more horizontally aligned and, consequently, a lower Haller index (HI) of their chests (see Figure 2A). In turn, an increase of the ribs angle is associated with both an increase both in the rib fracture risk and in the thoracic stiffness.[42,44] Note that these previous findings on chest stiffness and rib fracture risk are in qualitative agreement with the present simulation results. For a given target compression depth, Equation (7b) tells us that the required compression force, and thus the apparent thoracic stiffness, would increase with decreasing HI. Likewise, according to Equation (8b) the maximum stress levels in the ribs, and thus the probability of a risk fracture during CPR, would increase with decreasing D_T.

4.1 | Study limitations

The model used in the present study shares most of the limitations previously noted by Suazo et al.[15] The main limitation of the present study is most probably the absence in the geometry model of the thoracic cage internal organs and soft tissues. Even if the mechanical stiffness of the rib cage structure is responsible for most of the resistance to compression during a CPR maneuver, the contribution to chest stiffness of internal organs and tissues, and particularly of the heart itself, might also be significant. Moreover, as the size, shape and stiffness of the heart might be roughly uncorrelated from rib cage dimensions, it is clear that the effect of variations of the heart characteristics on CPR performance needs to be carefully addressed in future investigations.

The present study does not consider two of the most relevant changes on the ribs features with age, namely the thinning of the ribs and the change (deterioration) of the osseous tissue mechanical properties. In regard of the increasing risk of rib fracture with age during CPR, these two factors are well aligned with the effects of changes in chest morphology (higher θ leading to lower HI and D_T) discussed above. However, both rib thinning and material deterioration result in a decrease, not an increase, of the overall chest stiffness. Thus, in regard of chest stiffness these two factors compensate for the progressive increase of the ribs angle with age, to the point that chest stiffness is said to be statistically independent of the patient's age.[42] It might be for the same reason that the measured compression force required for a target CPR depth was found not to depend on the patient's age.[46]

Another limitation is that we simulate an idealized CPR compression maneuver in which practical factors, such as the accumulated fatigue of the tissues as the real CPR advances cyclically in time, are ignored. Moreover, even if the present results might hint into some qualitative relations between the patients' rib cage dimensions and the chances of success of CPR maneuvers, reality is obviously very complex. The chances of return of spontaneous circulation and survival of a CPR patient depend on multiple factors, some of which lay far beyond the scope of the present study.

5 | CONCLUSIONS AND FUTURE WORK

Finite element simulations of the rib cage compression during a CPR maneuver have been carried out to elucidate the dependence of the achieved compression depth (ΔY) on the rib cage dimensions. At a given compression force level (F), the achieved compression depth increases with rib cage width (W_R) and decreases with both rib cage depth (L_R) and height (H_R). Consequently, the compression force required to achieve a target depth during CPR is found to decrease with increasing W_R and to increase with increasing L_R and H_R. Most interestingly, it has been found that a fairly good fit of the current predictions can be obtained by using only two quantities based on the rib-cages dimensions, which are the Haller index (HI) and the vertical sagittal cross-area (A_{YZ}). In particular, there is a strong positive dependence of ΔY on HI. That is, a higher (lower) ΔY would be achieved for patients having a higher (lower) HI. Similarly, for a mechanically assisted CPR, performed at a fixed target ΔY, a lower (larger) F would be required for patients having higher (lower) HI. Moreover, present results also suggest that, for a target ΔY level, patients with wider chests (larger W_R) would experience lower levels of stress in the osseous ribs as a consequence of the compression. Notwithstanding, this result must be taken with caution as there is still a long way to go between the mappings of stress levels on the ribs and a reliable prediction of the risk of rib fractures during CPR.

A future research based on empirical CPR data would be most helpful to properly test the main trends obtained in the present study. In the present FE study, we simulated a sample of patients whose chest geometries were uniformly distributed along each of the three spatial directions. In an empirical study, the measurements on CPR patients may be distributed otherwise and, consequently, a large fraction of individuals in a sample might be clustered within a relatively narrow region in the geometrical parameter space. A very large variability between individuals was reported in previous experimental studies for the relation between CPR compression depth and the applied force.[46–48] Moreover, the empirical data in these studies, obtained from in vivo CPR procedures, did not include the patients' complete chest geometry. In other words, such in vivo empirical data, even though very valuable in several aspects, could not be used to infer the dependence of rib cage mechanics during CPR on rib cage geometry. Future studies on the subject would therefore require the use of a comprehensive enough database that is, one containing not only the achieved compression depth and applied force during CPR but the complete physical dimensions of the rib cage for each patient as well. Also, prior to endeavoring any statistical study the database should be carefully analyzed to establish possible correlations between parameters (e.g., between rib cage width and depth) or significant departures from the (commonly assumed) normal distribution of the patient population (for example, having a significant portion of obese patients in a database might introduce bimodality in the distribution of rib cage depth). Ideally, the empirical CPR database should also contain data on the location and size of the patients' heart. In future FE simulations of CPR maneuvers, internal organs and tissues—particularly, the lungs and the heart—should be incorporated into the geometry model. Hence, not only would the global stiffness of the chest be more accurately characterized but, most importantly, it would be possible to predict the level of compression achieved within the different sections of the heart.

ACKNOWLEDGMENTS

This work was supported by Universitat Rovira i Virgili under grant 2018PFR-URV-B2-29.

CONFLICT OF INTEREST STATEMENT

The authors declare no conflict of interest.

DATA AVAILABILITY STATEMENT

No data to be shared.

ORCID

Josep M. López https://orcid.org/0000-0001-7541-8936
Youcef Azeli https://orcid.org/0000-0003-3558-124X

REFERENCES

1. Gräsner J-T, Lefering R, Koster RW, et al. EuReCa ONE 27 nations, ONE Europe, ONE registry: a prospective one month analysis of out-of-hospital cardiac arrest outcomes in 27 countries in Europe. *Resuscitation*. 2016;105:188-195.
2. Kouwenkhoven WB, Jude JR, Knickerbocker GG. Closed-chest cardiac massage. *JAMA*. 1960;173(10):1064-1067.
3. Handley AJ. Press hard – but perhaps not too hard. *Resuscitation*. 2014;85(2):153-154. doi:10.1016/j.resuscitation.2013.11.016
4. Stiell IG, Brown SP, Nichol G, et al. What is the optimal chest compression depth during out-of-hospital cardiac arrest resuscitation of adult patients? *Circulation*. 2014;130(22):1962-1970.
5. Berg RA, Hemphill R, Abella BS, et al. Part 5: adult basic life support: 2010 American Heart Association guidelines for cardiopulmonary resuscitation and emergency cardiovascular care. *Circulation*. 2010;122(18_suppl_3):S685-S705. doi:10.1161/CIRCULATIONAHA.110.970939
6. Beom JH, You JS, Kim MJ, et al. Investigation of complications secondary to chest compressions before and after the 2010 cardiopulmonary resuscitation guideline changes by using multi-detector computed tomography: a retrospective study. *Scand J Trauma Resusc Emerg Med*. 2017;25(8):1-7. doi:10.1186/s13049-017-0352-6
7. Azeli Y, Lorente Olazabal JV, Monge García MI, Bardají A. Understanding the adverse hemodynamic effects of serious thoracic injuries during cardiopulmonary resuscitation: a review and approach based on the Campbell diagram. *Front Physiol*. 2019;10(1475):1-6. doi:10.3389/fphys.2019.01475
8. Azeli Y, Barbería E, Fernández A, García-Vilana S, Bardají A, Hardig BM. Chest wall mechanics during mechanical chest compression and its relationship to CPR-related injuries and survival. *Resuscitation Plus*. 2022;10:100242. doi:10.1016/j.resplu.2022.100242
9. Karasek J, Slezak J, Stefela R, et al. CPR-related injuries after non-traumatic out-of-hospital cardiac arrest: survivors versus non-survivors. *Resuscitation*. 2022;171(February):90-95. doi:10.1016/j.resuscitation.2021.12.036
10. Duval S, Pepe PE, Aufderheide TP, et al. Optimal combination of compression rate and depth during cardiopulmonary resuscitation for functionally favorable survival. *JAMA Cardiol*. 2019;4(9):900-908.
11. Wang C-H, Huang C-H, Chang W-T, et al. Associations between body size and outcomes of adult in-hospital cardiac arrest: a retrospective cohort study. *Resuscitation*. 2018;130:67-72.
12. Galatianou I, Karlis G, Apostolopoulos A, et al. Body mass index and outcome of out-of-hospital cardiac arrest patients not treated by targeted temperature management. *Am J Emerg Med*. 2017;35(9):1247-1251.
13. Matinrazm S, Ladejobi A, Pasupula DK, et al. Effect of body mass index on survival after sudden cardiac arrest. *Clin Cardiol*. 2018;41(1):46-50.
14. Lee H, Oh J, Lee J, et al. Retrospective study using computed tomography to compare sufficient chest compression depth for cardiopulmonary resuscitation in obese patients. *J Am Heart Assoc*. 2019;8(23):e013948.
15. Suazo M, Herrero J, Fortuny G, Puigjaner D, López JM. Biomechanical response of human rib cage to cardiopulmonary resuscitation maneuvers: effects of the compression location. *Int J Numer Methods Biomed Eng*. 2022;38(4):e3585.
16. Mitsuhashi N, Fujieda K, Tamura T, Kawamoto S, Takagi T, Okubo K. BodyParts3D: 3D structure database for anatomical concepts. *Nucleic Acids Res*. 2009;37(Suppl. 1):D782-D785. doi:10.1093/nar/gkn613
17. Code_Aster, structures and thermomechanics analysis for studies and research. Electricité de France; 2018. www.code-aster.org
18. Forman, J. L. *The Structural Characteristics of the Costal Cartilage: the Roles of Calcification and the Perichondrium, and the Representation of the Costal Cartilage in Finite Element Models of the Human Body*. Ph.D. Dissertation. University of Virginia School of Engineering and Applied Science, Department of Mechanical and Aerospace Engineering. 2009.
19. Lau A, Kindig M, Salzar R, Kent R. Micromechanical modeling of calcifying human costal cartilage using the generalized method of cells. *Acta Biomater*. 2015;18:226-235.
20. McCormick WF. Mineralization of the costal cartilages as an indicator of age: preliminary observations. *J Forensic Sci*. 1980;25(4):736-741.
21. Lau A, Oyen ML, Kent RW, Murakami D, Torigaki T. Indentation stiffness of aging human costal cartilage. *Acta Biomater*. 2008;4:97-103. doi:10.1016/j.actbio.2007.06.008
22. Forman JL, Kent RW. The effect of calcification on the structural mechanics of the costal cartilage. *Comput Methods Biomech Biomed Engin*. 2014;17(2):94-107. doi:10.1080/10255842.2012.671307
23. Yi W, Heo M, Lee S, Choi S, Huh K, Lee S. Direct measurement of trabecular bone anisotropy using directional fractal dimension and principal axes of inertia. *Oral Maxillofac Radiol*. 2007;104(1):110-116. doi:10.1016/j.tripleo.2006.11.005

24. Maggiano IS, Maggiano CM, Clement JG, Thomas CDL, Carter Y, Cooper DML. Three–dimensional reconstruction of Haversian systems in human cortical bone using synchrotron radiation–based micro–CT: morphology and quantification of branching and transverse connections across age. *J Anat*. 2016;228:719-732. doi:10.1111/joa.12430
25. Toniolo I, Salmaso C, Bruno G, et al. Anisotropic computational modelling of bony structures from CT data: an almost automatic procedure. *Comput Methods Prog Biomed*. 2020;189:105319. doi:10.1016/j.cmpb.2020.105319
26. Baier W, Norman DG, Williams MA. Micro-CT for the examination of paediatric rib injuries: a case series. *Forensic Sci Int*. 2021;325:110789. doi:10.1016/j.forsciint.2021.110789
27. Hashiguchi K. *Elastoplasticity Theory*. 2nd ed. Springer; 2014.
28. Xiao H, Bruhns OT, Meyers A. Elastoplasticity beyond small deformations. *Acta Mech*. 2006;182:31-111. doi:10.1007/s00707-005-0282-7
29. Kindig M, Lau AG, Kent RW. Biomechanical response of ribs under quasistatic frontal loading. *Traffic Inj Prev*. 2011;12(4):377-387. doi:10.1080/15389588.2011.583960
30. Kindig M, Li Z, Kent R, Subit D. Effect of intercostal muscle and costovertebral joint material properties on human ribcage stiffness and kinematics. *Comput Methods Biomech Biomed Engin*. 2015;18(5):556-570. doi:10.1080/10255842.2013.820718
31. Rebeis EB, de Campos JRM, Fernandez Â, Moreira LFP, Jatene FB. Anthropometric index for pectus excavatum. *Clinics*. 2007;62(5):599-606.
32. Archer JE, Gardner A, Berryman F, Pynsent P. The measurement of the normal thorax using the Haller index methodology at multiple vertebral levels. *J Anat*. 2016;229:577-581. doi:10.1111/joa.12499
33. Liu J-Z, Ye S, Cheng T, et al. The effects of thoracic cage dimension and chest subcutaneous adipose tissue on outcomes of adults with in-hospital cardiac arrest: a retrospective study. *Resuscitation*. 2019;141:151-157.
34. Laurin L-P, Jobin V, Bellemare F. Sternum length and rib cage dimensions compared with bodily proportions in adults with cystic fibrosis. *Can Respir J*. 2012;19(3):196-200.
35. Pickard A, Darby M, Soar J. Radiological assessment of the adult chest: implications for chest compressions. *Resuscitation*. 2006;71(3):387-390. doi:10.1016/j.resuscitation.2006.04.012
36. Doblaré M, García JM, Gómez MJ. Modelling bone tissue fracture and healing: a review. *Eng Fract Mech*. 2004;71:1809-1840. doi:10.1016/j.engfracmech.2003.08.003
37. Cavanaugh JE, Neath AA. The Akaike information criterion: background, derivation, properties, application, interpretation, and refinements. *WIREs Comput Stat*. 2019;11:e1460. doi:10.1002/wics.1460
38. Kralj E, Podbregar M, Kejžar N, Balažic J. Frequency and number of resuscitation related rib and sternum fractures are higher than generally considered. *Resuscitation*. 2015;93:136-141. doi:10.1016/j.resuscitation.2015.02.034
39. Azeli Y, Barbería E, Jiménez-Herrera M, Ameijide A, Axelsson C. Serious injuries secondary to cardiopulmonary resuscitation: incidence and associated factors. *Emergencias*. 2019;31:327-334.
40. Hoke RS, Chamberlain D. Skeletal chest injuries secondary to cardiopulmonary resuscitation. *Resuscitation*. 2004;63:327-338. doi:10.1016/j.resuscitation.2004.05.019
41. Holcombe SA, Wang SC, Grotberg JB. The effect of age and demographics on rib shape. *J Anat*. 2017;231(2):229-247.
42. Kent R, Lee S-H, Darvish K, et al. Structural and material changes in the aging thorax and their role in crash protection for older occupants. SAE Technical Paper 2005.
43. Gayzik FS, Yu MM, Danelson KA, Slice DE, Stitzel JD. Quantification of age-related shape change of the human rib cage through geometric morphometrics. *J Biomech*. 2008;41:1545-1554. doi:10.1016/j.jbiomech.2008.02.006
44. Weaver AA, Schoell SL, Stitzel JD. Morphometric analysis of variation in the ribs with age and sex. *J Anat*. 2014;225(2):246-261.
45. Wang Y, Cao L, Bai Z, et al. A parametric ribcage geometry model accounting for variations among the adult population. *J Biomech*. 2016;49:2791-2798. doi:10.1016/j.jbiomech.2016.06.020
46. Tomlinson AE, Nysaether J, Kramer-Johansen J, Steen PA, Dorph E. Compression force—depth relationship during out-of-hospital cardiopulmonary resuscitation. *Resuscitation*. 2007;72:364-370. doi:10.1016/j.resuscitation.2006.07.017
47. Gruben KG, Guerci AD, Halperin HR, Popel AS, Tsitlik JE. Sternal force-displacement relationship during cardiopulmonary resuscitation. *ASME J Biomech Eng*. 1993;115(May):195-203. doi:10.1115/1.2894121
48. Beesems SG, Hardig BM, Nilsson A, Koster RW. Force and depth of mechanical chest compressions and their relation to chest height and gender in an out-of-hospital setting. *Resuscitation*. 2015;91:67-72. doi:10.1016/j.resuscitation.2015.03.020

How to cite this article: Moradicheghamahi J, Fortuny G, López JM, Puigjaner D, Herrero J, Azeli Y. The effect of thoracic dimensions on compression depth during cardiopulmonary resuscitation. *Int J Numer Meth Biomed Engng*. 2023;39(7):e3718. doi:10.1002/cnm.3718